The potential of spectral unmixing method applied to PRISMA hyperspectral images in the identification of Li minerals: an evaluation for prospecting purposes

D. Santos, J. Cardoso-Fernandes, A. Lima, A. Teodoro

D. Santos, J. Cardoso-Fernandes, A. Lima, A. C. Teodoro, "The potential of spectral unmixing method applied to PRISMA hyperspectral images in the identification of Li minerals: an evaluation for prospecting purposes," Proc. SPIE 12268, Earth Resources and Environmental Remote Sensing/GIS Applications XIII, 1226811 (26 October 2022); doi: 10.1117/12.2636034

SPIE.

Event: SPIE Remote Sensing, 2022, Berlin, Germany

The potential of spectral unmixing method applied to PRISMA hyperspectral images in the identification of Li minerals: A evaluation for prospecting purposes

Santos, D.[1,2] , J. Cardoso-Fernandes[1,2], Lima, A.[1,2], Teodoro, A.C.*[1,2],

[1]Institute of Earth Sciences, FCUP pole, Porto, Portugal; [2] Department of Geosciences, Environment and Spatial Planning Faculty of Sciences of the University of Porto, Portugal; *amteodor@fc.up.pt

ABSTRACT

Different remote sensing methods already applied have proven efficient in identifying pegmatites, but the high number of the false positives and the size of the study areas involved, make the location of new points of interest for exploration a difficult task. In order to develop and evaluate more autonomous tools for localization of new points of interest, this study aims to apply the Envi Spectral Hourglass Wizard (SHW) algorithm and spectral analysis, both applied on PRISMA hyperspectral images, to determine mineral distribution in St. Austell greisen deposit, a Li exploration target located at Cornwall, UK. The SHW finds endmembers within the dataset to map their location and sub-pixel abundance. This processing workflow is composed of several steps: (i) MNF (Minimum Noise Fraction) Transform; (ii) PPI (Pixel Purity Index); (iii) n-D space visualizer, allowing the extraction of the endmembers and; (iv) the SAM (Spectral Angle Mapper) classification algorithm, which classifies the image creating a class for each collected endmember. The classification results show the potential of the method to indicate the presence of Li minerals being able to identify Kaolinite and map the distribution and abundance of Topaz, Tourmaline and Biotite. This approach is highly valuable for the Li mining industry.

Keywords: MTMF; SAM; Li minerals; Spectral Hourglass Wizard; PRISMA satellite.

1. INTRODUCTION

The failure of the TERRA ASTER SWIR module has left a gap in remote sensing data for scientific geologic prospecting research. This makes new hyperspectral sensors of great interest for this scientific field. This is the case of the hyperspectral satellite PRISMA. Launched on 2019[1], the PRISMA hyperspectral data has been used for research in the areas of agriculture[2], fire mapping[3], and water applications[4]. But few studies have been done concerning geological resources. A preliminary study in the St. Austell region that applies spectral unmixing methods and band calculations on hyperspectral PRISMA images aimed to identify Topaz[5]. However, others research with hyperspectral data were conducted in this study area. Ellis and Scott[6], conducted, on 2004, a study focused in the use of airborne hyperspectral data to map the distribution of Granite minerals and hydrothermal alteration assembles. Mujabar and Dajkumar[7] used hyperspectral data to map Bauxite mineral deposits at Saudi Arabia. The last two references mentioned researches that applied spectral unmixing methods on hyperspectral data to find endmembers and map mineral abundance, however, more studies about this method applied to PRISMA hyperspectral data is needed. This research tries to go forward and aims to apply the Spectral Hourglass Wizard (SHW) method on PRISMA hyperspectral images to find minerals of interest and verify its potential for the prospection of Li minerals. The study area is therefore the St. Austell China clay region in South West England (Cornwall). Six types of Granite can be found in St. Austell pluton, which is a major source of high-quality Kaolin[8]. Although may not be suitable for multispectral data, the SHW method is one of the most applied image processing techniques for processing hyperspectral images[9]. This method starts by reducing the dimensionality of the data through the application of Minimum Noise Fraction (MNF), data dimensionality, and Pixel Purity Index (PPI). After this, the n-D visualizer is used to select and, retrieve the endmembers, and, in sequence, a spectral match is performed between the endmembers extracted in the n-D space visualizer and the USGS spectral library. The next step is to apply two classification methods. The Mixture Tuned Matched Filtering (MTMF) that is based on partial unmixing, and a physical-based spectral classification algorithm called Spectral Angle Map Creator (SAM).

Earth Resources and Environmental Remote Sensing/GIS Applications XIII, edited by Karsten Schulz, Ulrich Michel, Konstantinos G. Nikolakopoulos, Proc. of SPIE Vol. 12268, 1226811

2. STUDY AREA

Located in South West England (Cornwall), the St. Austell China clay region (figure 1), is a major source of high-quality Kaolin[8]. Six types of Granite can be found in St Austell pluton,namely: (i) Biotite Granite, (ii) Lithium Mica Granite, (iii) Tourmaline Granite, (iv) Fine-grained Granite, and (v) Topaz Granite and Tourmaline Breccia Pipe[8,10]. Biotite Granite is the predominant lithology corresponding to 70% of the outcrops. Among the minerals that can be found in this outcrop, Uraninite, Rutile, Zircon, and Muscovite, can be highlighted. Although not being lithologically dominant as Biotite Granite, Lithium Mica Granite is similar in grain size and texture to Biotite Granite. Associated minerals include Apatite, Monazite and Zircon[8]. The Tourmaline Granite contains large Quartz grains, Plagioclase, Apatite and Tourmaline. The associated minerals in Fine-grained Granite include Monazite, Zircon, and Rutile. Containing a smaller mineral paragenesis than the other Granites, the Topaz Granite contains Zircon, Amblygonite, and Apatite[8].

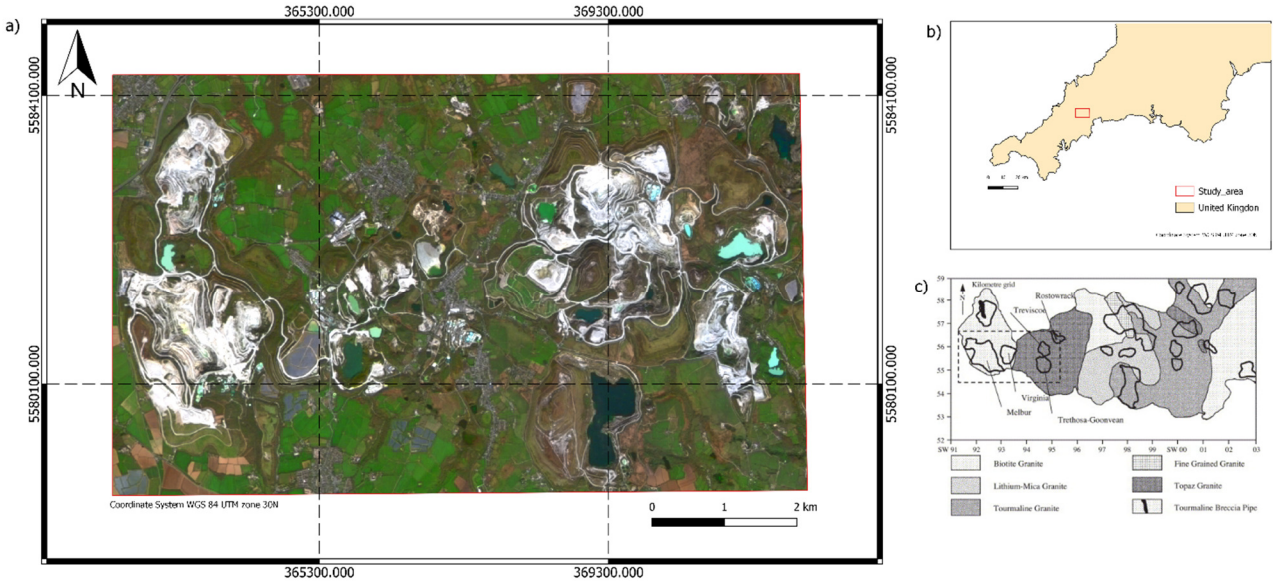

Figure 1. Study Area Location. a) PRISMA High-resolution (5 m) tur color RGB composition of the St. Austell China clay region. b) Location of the study area in SW England. c) Lithological map of the study area[6].

3. METHODOLOGY

3.1 Data and preprocessing

Launched on 22 March 2019, the PRISMA pushbroom sensor has 239 hyperspectral bands in a spectral range between 400-2500 nm with 30 m of spatial resolution (5 m for Panchromatic band), and a revisit time of approximately 29 days. Of the 239 bands, 66 correspond to Visible and Near Infrared region (VNIR: 400-1010 nm) and 173 to the Short Wave Infrared region (SWIR: 920-2505 nm) spectrum[1,11]. A product collected on 05/04/2020, with a cloud coverage of 3,27% was downloaded from the PRISMA Mission Catalog website (https://prisma.asi.it/). This product was acquired at the L2D level, and available at surface reflectance.The HDF-EOS5 (Hierarchical Data Format - Earth Observing System) file was processed in ENVI 5.6.2 software and a Color Normalized (Brovey) Sharpening was performed to obtain a true color composite with 5 m GSD (Fig. 1). After the image acquisition, some preprocessing steps were necessary. To avoid duplication between the VNIR and SWIR bands, the overlap bands between 920 and 1010 nm were excluded. For that, a new raster stack was generated with 221 bands (59 bands in the VNIR cub and 162 bands in the SWIR cub). This procedure is necessary to avoid spectral confusion. Mineral spectra from the USGS spectral library[12] were used as the basis for building a spectral library resampled to the PRISMA spectral resolution. First, only the minerals of interest were selected from the USGS spectral library and used to build a dedicated library. Then, the spectra were resampled to PRISMA resolution using the Spectral Library Resampling tool available in ENVI software, which allows resampled all spectra at once.

3.2 Spectral Hourglass Wizard (SHW)

The SHW is a spectral unmixing method workflow that guides step-by-step through the ENVI hourglass process workflow to find and map endmembers from hyperspectral or multispectral data[13]. First, the data to be used as input must be selected. In this study, the staking made with 221 bands (without the overlap bands) was used as input. After that, the process was divided into three phases. The first consisted of a series of methods to reduce the dimensionality of the data, both in spectral and spatial terms. In this step, the MNF, Data Dimensionality, and the Pixel Purity Index (PPI) methods were applied. The second phase consisted of extracting the endmembers from the image through the n-D Visualizer. The endmembers retrieved with the n-D Visualizer were then analyzed with the Spectral Analyst tool to select which should be used in the classification step. After identifying the endmembers of interest, a more specific analysis was performed, comparing the selected endmembers with the pure spectra from the resampled USGS spectral library to further prepare for SAM and MTMF classification. This analysis aimed to verify the potential of the SHW method in identifying six minerals of interest (Kaolinite, Lepidolite, Muscovite, Biotite, Topaz and Tourmaline). At last, two classification algorithms (SAM and MTMF) were applied to map the distribution and abundance of the endmembers in the image. Figure 2 present the methodology followed in this work

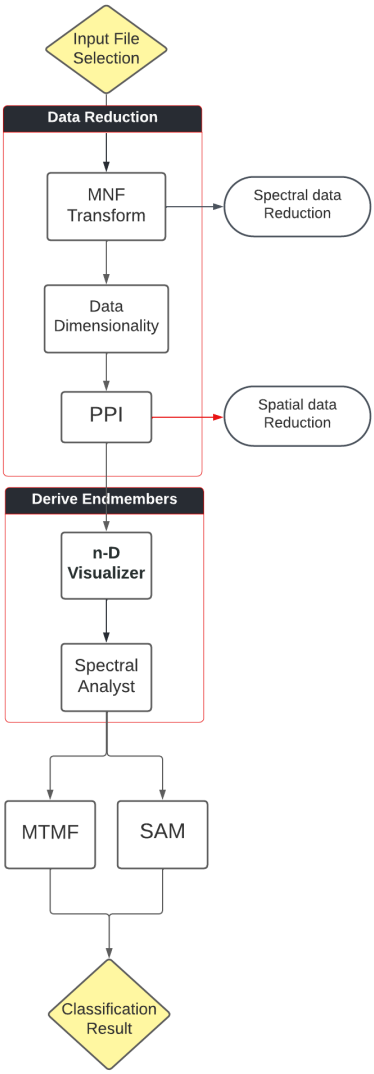

Figure 2. Workflow of the methodology employed in this work.

3.2.1 Minimum Noise Fraction (MNF)

After selecting the appropriate input to be used in the SHW approach, different methods were applied to reduce the dimensionality of the hyperspectral imagery. The first was the MNF Transform. The MNF is used to segregate and equalize the noise in the data, describe the inherent dimensionality of data and reduce the computational requirements for subsequent processing[7,14,15]. The high information content is concentrated in the lower numbered bands (called coherent images), while the last bands concentrate the noise[6]. The process of determining the threshold that separates signal bands from noise is called spatial coherence[16]. An MNF transform was performed for all 221 bands in VNIR and SWIR region (400-2500 nm). Figure 3 shows the plot of Eigenvalues for different MNF bands (Eigen number). Knowing that when the eigenvalues are close to 1 only noise is left in the transformed band, it is possible to see that the threshold is around MNF band 20[16].

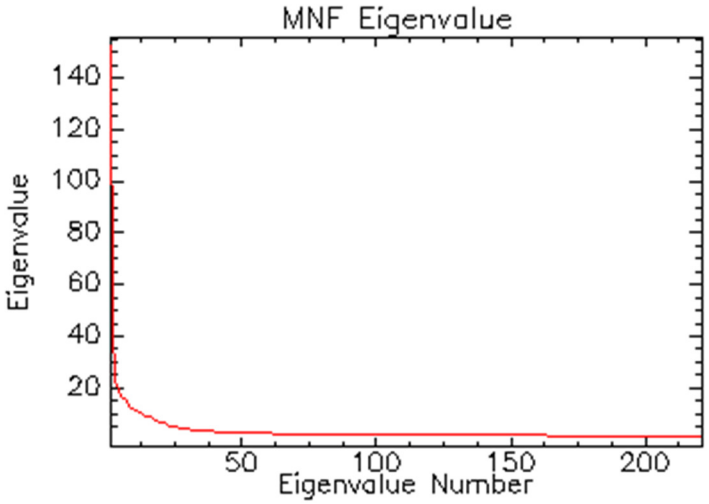

Figure 3. Eigenvalue plot for different MNF bands (Eigen number). The Y axis indicates the higher data variance in the transformed band. Eigenvalues close to 1, represent noisy bands.

3.2.2 Data Dimensionality

Through SHW it is also possible to determine, in a more accurate way, the spatial coherence through the Data Dimensionality panel[16]. The Data Dimensionality panel indicates several coherent bands, allowing the user to modify the threshold level to separate the signal from noise. As indicated in Figure 4, the threshold level applied was 80, and the number of coherent images according to this threshold level is 24.

3.2.3 Pixel Purity Index (PPI)

The PPI was applied to find the most spectrally pure pixels. This method aims to achieve the spectral unique target minerals by reducing the number of pixels in the data through a spectral redundancy analysis of data to obtain the most spectrally pure pixels[7,15]. The PPI analysis was performed considering 10,000 iterations with a threshold value of 3.0. The plot in Figure 5 shows the relationship between the number of interactions and the number of pixels found to be extreme. The curve is steeply in the beginning, as new pixels are found in each iteration, and flatten out when the extreme pixels are found.

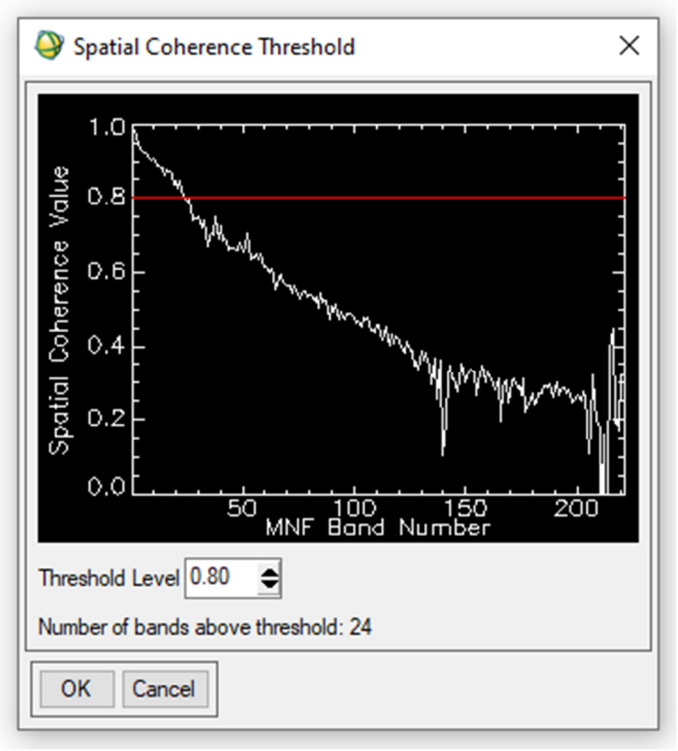

Figure 4. Data Dimensionality analysis. The red line represents the Threshold level.

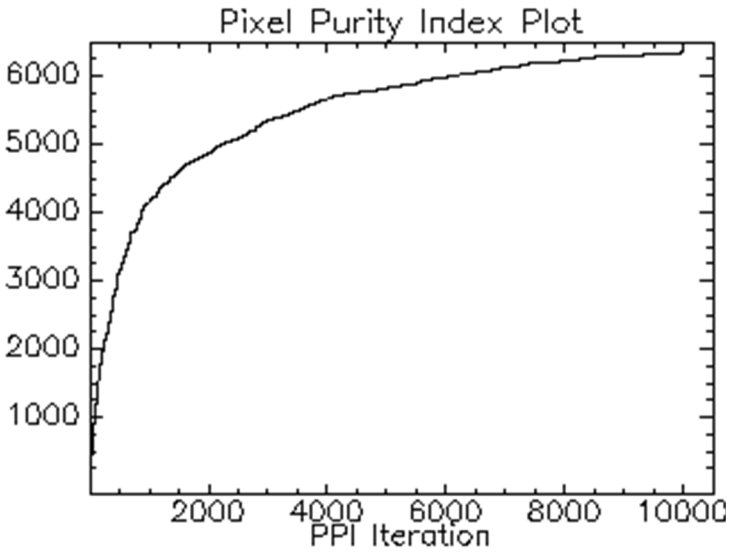

Figure 5. PPI plot.

3.2.4 n-D Visualiser

The n-dimensional visualizer (n-D Visualiser) is used to extract the endmembers from the image subset[9,17,18]. After deriving the endmembers from PPI, a scatter plot was computed. The spectra are represented by points of the data cloud and the *n*

represents the number of bands[19]. The n-D Visualiser allows mapping endmembers by clusters. The panel automatically selects endmembers by forming pre-clusters. In this search, 25 endmembers were automatically selected. Knowing that the most spectrally unique material in the image lies at the tips of the data cloud[19], seven classes were defined at these tips and their endmembers were extracted to be used in the classification. After the reflectance spectra of the selected endmembers were evaluated to determine and understand which elements should be selected. The retrieved endmembers were compared to pure spectra from the resampled USGS spectral library through the spectral analyst tool. The spectral analyst tool uses the Spectral Feature Fitting (SFF) algorithm to rank the match of an unknown spectrum to the ones in the spectral library[20]. This analysis was done with the average of the endmembers of each class that the n-D Visualizer automatically provides (Figure 6).

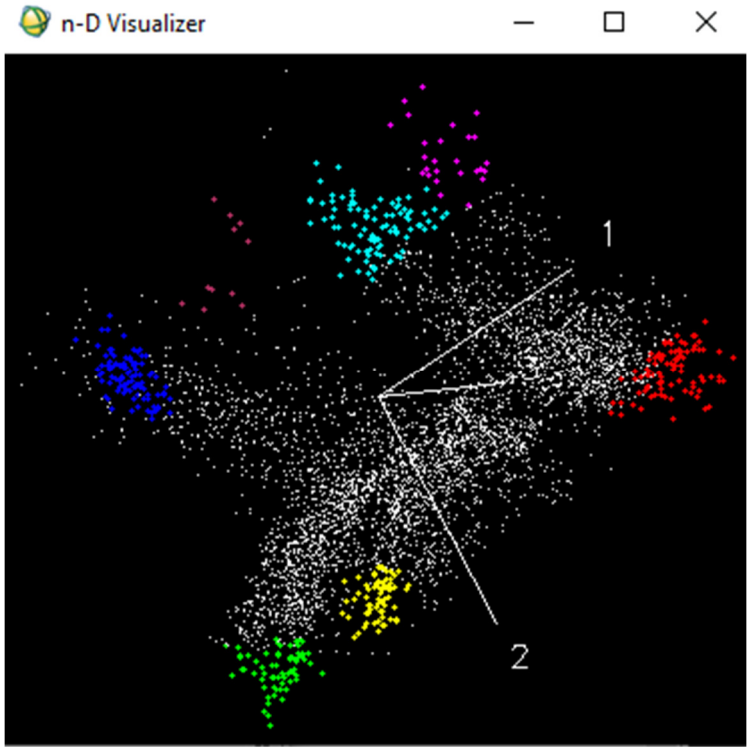

Figure 6. n-D Visualiser scatters plot. Each point on the data cloud represents a spectrum. The distinct colors represent the seven classes defined at the tips of the cloud.

3.2.5 Mixture Tuned Matched Filtering (MTMF)

The MTMF performs Matched Filtering (MF) and uses infeasibility images to reduce the number of false positives that appear when the MF is used[6,21]. The MF finds abundances of a defined endmember by partial unmixing, maximizing the response of the defined endmember and suppressing the response of the composite unknown background[21]. The MTMF results in a set of rule images corresponding to both the MF score and the infeasibility score for each pixel compared to each endmember. The infeasibility score indicate the feasibility of the MF result, therefore, correctly mapped pixels have a low infeasibility score and a MF score above the background distribution of about zero. Using the endmembers retrieved through n-D Visualiser, MTMF resulted in seven MF bands that were used for analysis in a GIS environment.

3.2.6 Spectral Angle Map Creator (SAM)

Defined as a physically-based spectral classification, the SAM algorithm uses an n-D angle to match pixels to reference spectra, comparing the angle between the endmember spectrum vector and each pixel vector in n-D space[22]. Pixels furthest from the maximum angle threshold specified in radians are not classified while smaller angles represent closer matches to

the reference spectrum[22]. The SAM classification results provided multiple clusters of probable target pixels, that helped analyze the distribution of the elements under study[23]. The maximum angle chosen for classification was 0.10.

4. RESULTS AND DISCUSSION

4.1 MNF Transform

By adding MNF bands on the red, blue, and green channels it is possible to realize RGB combinations of bands that assigns similar colors to areas within the scene with similar spectral responses (Figure 7). This allows to analyze the variation in mineral abundance[6]. The RGB combination of MNF 432 shows the same color pattern (yellow, orange, and red) for the exploration area. This may indicate little spectral variety of minerals in the studied region.

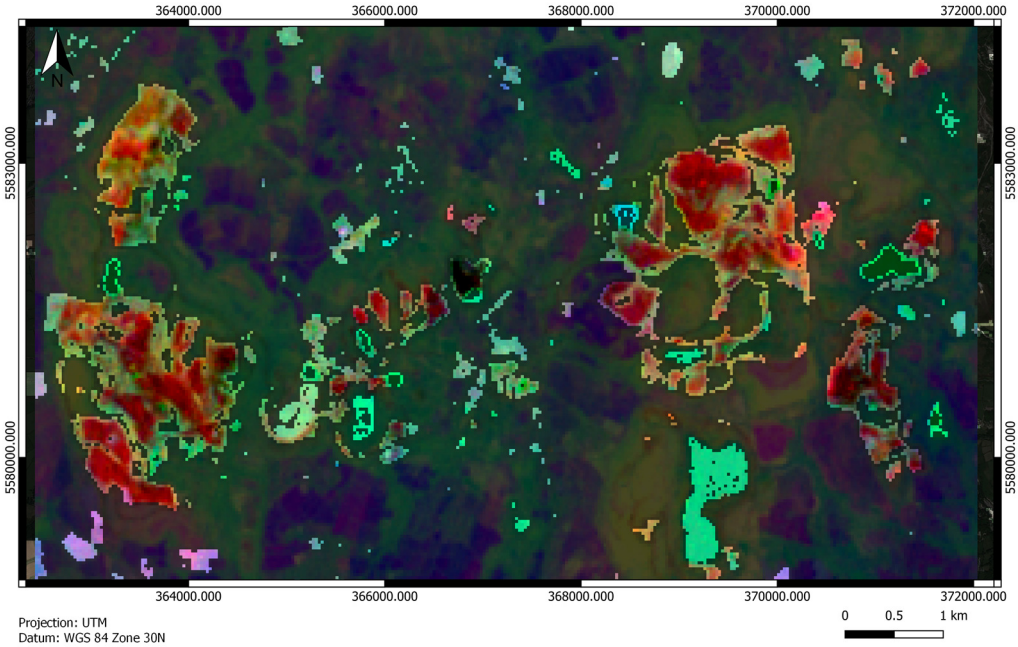

Figure 7. RGB 432 combination of MNF bands with a vegetation mask. Similar colors indicate similar spectral responses. The mining area is highlighted in reddish tones. Water in green tones.

4.2 n-D Visualizer

Figure 8 presents the analysis made of the mean surface reflectance obtained by the n-D Visualizer. Through this analysis, it was possible to separate spectra belonging to vegetation from spectra that might be minerals of interest. In the spectra marked as vegetation, in Figure 8 it is possible to see the double absorption (~500 nm and ~670 nm) that are characteristic of chlorophyll. The reflectance peak in the NIR region (~770 nm) corresponds to light reflectance by leaf pigments. These characteristic features indicate that the classes N-D Class 1, n-D Class 2, and n-D Class 4 correspond to vegetation[24]. The spectra noted as minerals in Figure 8, in turn, have two absorptions of Aluminium monohydroxide - AlOH (~2160 nm and ~2206 nm) and one absorption of Magnesium hydroxide - MgOH (~2320 nm). These absorptions in the SWIR region can be characteristic OH-bearing silicates such as chlorite, white Mica or Clays, with the last commonly found in the spectra of Lithium minerals[25–27].

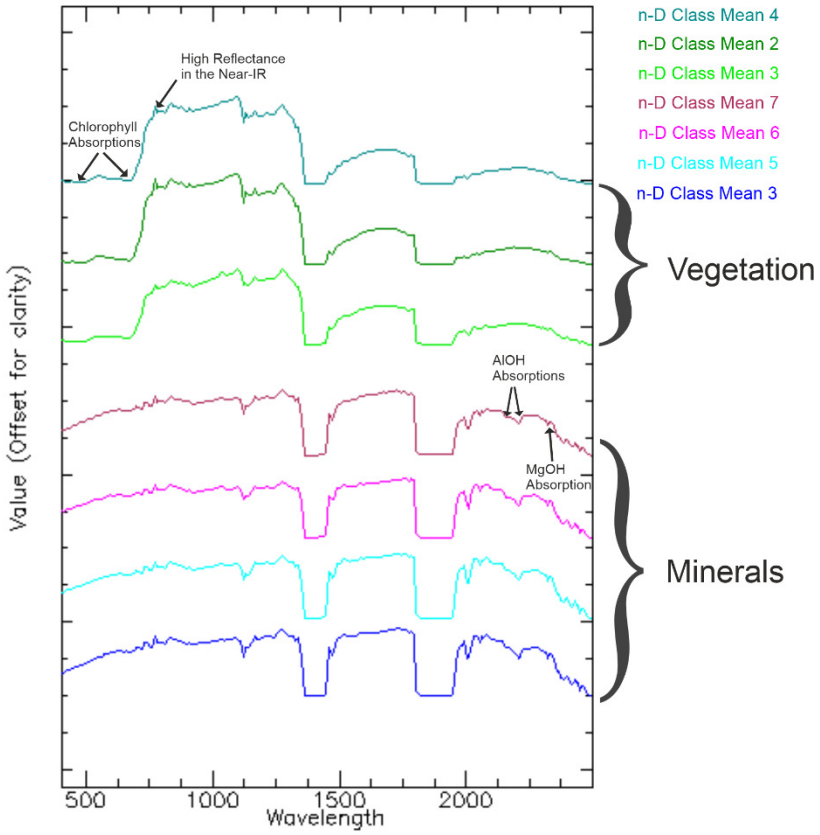

Figure 8. The reflectance of the average endmembers provided by the n-D Visualizer. The chlorophyll absorptions and peak reflectance in the NIR region identify the vegetation spectra. Characteristic absorptions feature of AlOH and MgOH in the SWIR region indicate the mineral spectra.

Adding the endmembers selected by the n-D Visualizer to a high-resolution true-color image from the PRISMA satellite (5 m), it is possible to map the location of the endmembers that have been selected in the data cloud. Taking into consideration that the mining area of the study region can be divided according to the different granulometry and mineralogy of the exploited Granite, we can understand the relationship between the selected classes in the n-D viewer and the dominant Granite type (Figure 9). n-D Class 7 corresponds to the endmembers found in the Topaz mining area (Figure 9-c). n-D Class 6 corresponds predominantly to the Tourmaline mining area, n-D Class 5 corresponds to an area that includes mining of various Granite types (fine Granite, Lithium Mica, Biotite, and Tourmaline), and the n-D class 3 corresponds to Biotite. N-D Class 1, n-D Class 2, and n-D Class 4 correspond to vegetation areas, as aforementioned. No endmembers were identified in urban areas, exposed soil, or water bodies. The identification of these elements is not the main objective of this study and a not interfere with the results. When the scatter plot (Figure9-b) is analyzed, it can be seen that the endmembers of n-D Class 5 and n-D Class 6 are very close in n-dimensional space. As a consequence of this, some endmembers of class 6 were erroneously selected as belonging to n-D Class 5. To attenuate this effect and to ensure maximum separability between the classes, the selection was redone until an acceptable result was obtained. Still, some endmembers continued to be misclassified among these classes.

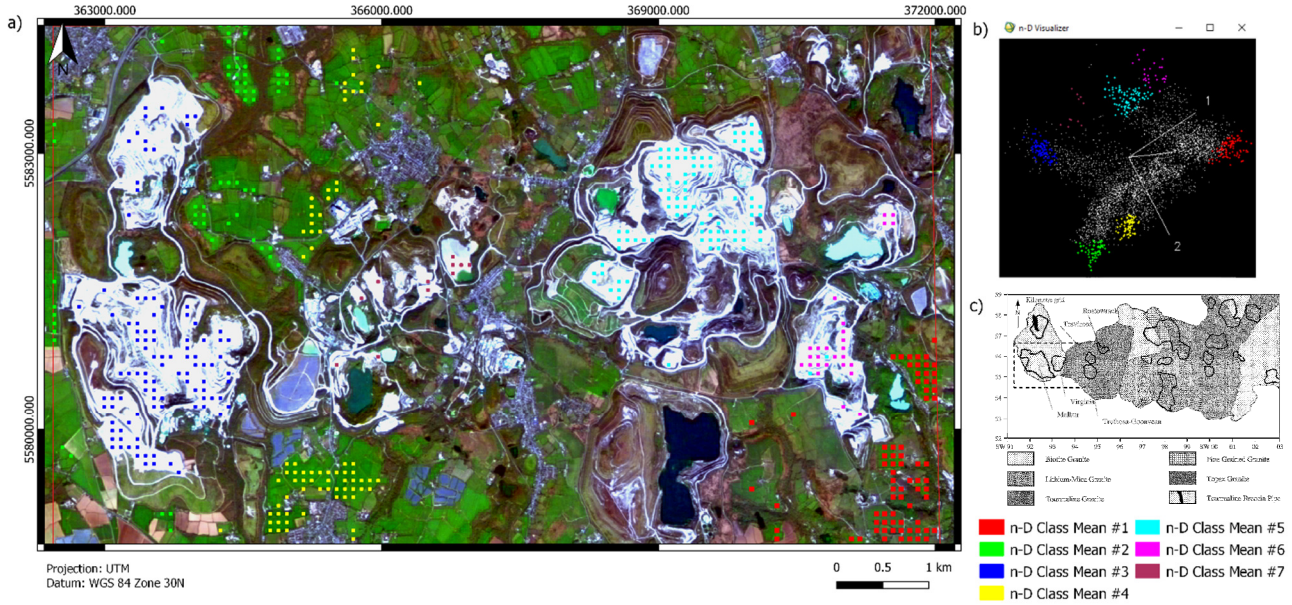

Figure 9. Location of the selected PPI in the study area. a) Distribution of the PPI of the elements present in the study area. b) Scatter plot representing the data cloud in n-dimensional space. The purest PPIs are at the corners of the graph. The colored clusters are the selected PPIs. c) Lithologic map of the study area, adapted from Ellis and Scott[6].

4.3 Spectral Analyst

After retrieving the selected endmembers from the data, it is possible to use the Spectral Analyst tool to identify minerals based on their spectral characteristics. A comparison between endmembers retrieved from the data and pure spectra from the USGS spectral library was made. Six minerals were selected for the analysis: Kaolinite, Lepidolite, Muscovite, Biotite, Topaz, and Tourmaline. However, the Spectral Analyst tool did not show high scores for any of the minerals studied, indicating that there is no high confidence in the spectral similarity between the endmembers and the spectra from the USGS spectral library. Nevertheless, as most of the diagnostic absorptions of the minerals are in the SWIR region, and the fact that the VNIR bands were also used in this analysis may also have contributed to this low score. To be able to evaluate the results more reliably, a comparison between the endmember spectrum and the selected library spectrum has been analyzed (Figure 10). From this analysis, it is possible to conclude that only Kaolinite was correctly identified by this method. The highest score for Kaolinite was from n-D Class 6 (0.184), but there is little difference from the scores for n-D Classes 3, 5, and 7, meaning that the endmembers of these classes are very similar. Table 1, shows the scores for each n-D class. When comparing the endmember of n-D class 6 with the pure spectrum we can notice two AlOH absorptions in the SWIR region (~2159 nm and ~2206 nm) this double absorption may indicate the presence of Kaolinite as identified by the results of the Spectral Analysis tool. All endmembers show score 0 for Biotite. This indicates that nothing similar to Biotite was detected among the endmembers. Lepidolite was identified with higher scores in the n-D classes that correspond to the vegetation. When looking at the comparison of the pure spectra and the endmembers it can be seen that the characteristic water/OH absorption of Lepidolite (~1405 nm)[28] is negatively impacted by the water vapor absorption bands of the atmosphere. This may have negatively impacted the identification of this mineral. The Muscovite obtained similar values to Kaolinite. However, when we analyze the spectra, we notice that, as with Lepidolite, one of its diagnostic absorptions also falls within the zone covered by the water vapor bands. In addition, the AlOH absorption (~2206 nm) is not deep enough to diagnose Muscovite. With a characteristic deep water/OH absorption (~1405 nm) affected by the water vapor absorption bands, the Topaz could not be accurately identified because the deep diagnostic absorption marked around 2080 nm that is not present in any of the endmembers, although some spectra present a small inflection at ~2075nm. Similar to Lepidolite, Tourmaline also scored high in all vegetation classes, indicating a wrong spectral match based on the diagnostic absorptions. This could be due to a similarity between the ferrous iron absorptions of Tourmaline in the VNIR region and the chlorophyll and leaf pigments of vegetation. Like others, the Tourmaline diagnostic absorption

around 1440 nm was impacted by the water vapor bands and none of the diagnostic FeOH and MgOH absorptions are present.

Table 1. Spectral Analyst results for Kaolinite.

Kaolinite	
N-D Class	Score
N-D Class Mean 6	0.184
N-D Class Mean 3	0.182
N-D Class Mean 5	0.179
N-D Class Mean 7	0.178
N-D Class Mean 4	0.128
N-D Class Mean 2	0.128
N-D Class Mean 1	0.124

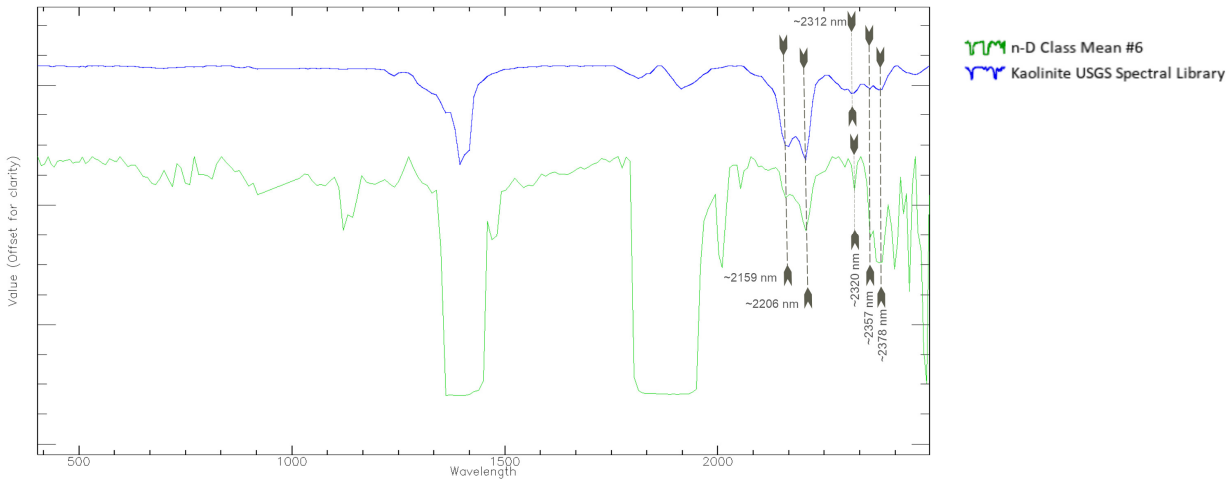

Figure 10. Comparison of the continuum removed endmember spectra (in green color) and the reference spectrum of the USGS spectral library (blue color). The double absorption (at 2159 nm and 2206 nm) together with the other three highlighted absorptions (at 2320 nm, 2357 nm, and 2378 nm) diagnose Kaolinite.

4.4 MTMF

Only the results of the n-D classes that correspond to minerals will be shown in this section. As can be seen in Figure 11, those classified by the MTMF can be divided according to the type of Granite present in the mining area. Figure 11-a) presents the classification of MF Score 3 (Biotite). The pixels occur in the area where Biotite Granite dominates. Some pixels were also classified in the center left side, as expected since it is a mixed area with several Granite types. Figure 11-b), shows the classification of MF Score 7 (Topaz). In this case, pixels were classified in the Topaz Granite location. This classification has the fewest number of classified pixels (269) and a few pixels have been classified in the left-center part of the image where there is no Topaz. Figure 11-c) presents MF score 6 (Tourmaline) classification and the pixels correspond to the area where Tourmaline Granite crops out. This is the second classification with the fewest pixels classified (293). Some pixels were classified in the left central part (mixed) and in the upper right corner, a region that coincides with a Tourmaline Breccia Pipe. Finally, Figure 11-d) shows MF score 5 (various types of Granites) classifications. The pixels were, mostly, classified in a mixed area, with the presence of several Granite types, and also classified pixels in the area of Tourmaline Granite, Topaz Granite, and, to a lesser extent, Biotite Granite. Table 2 shows the number of pixels classified per class.

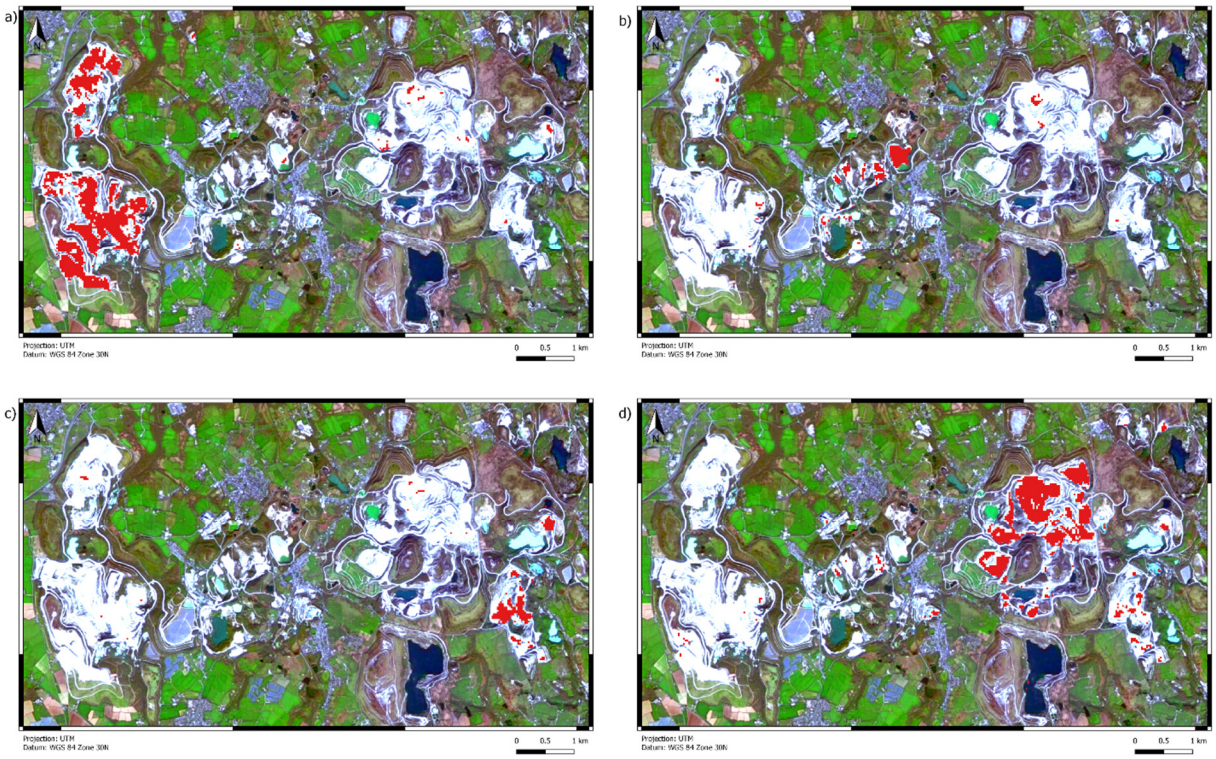

Figure 11. MTMF classification result. a) Classification result for the n-D class 3 (Biotite). Most of the pixels were classified in the Biotite Granite region. b) Classification result for the n-D class 7 (Topaz). Most of the pixels were classified in the Topaz Granite region. c) Classification result for the n-D class 6 (Tourmaline). Most of the pixels were classified in the Tourmaline Granite region. d) Classification result for the n-D class 5 (various types of Granites). Most of the pixels were classified in the mixed region.

Considering that Kaolinite is the mineral most present in all the selected endmembers and that they are all very similar to each other, it was surprising that this method can form clusters that coincide with the location of the different Granite types present in the study area. When comparing the results generated from the MF score with the location of the endmembers that were selected with the help of the data (Figure 9), we notice a pattern between the location of the endmembers grouped in the n-D classes and the clusters created by the MTMF method. This indicates that in addition to spectral similarities, this method also takes into account the geographic location of the endmembers used for classification. Although failing to distinguish elements in the mixed region, it still shows much potential in forming clusters that indicate the abundance of minerals of interest.

Table 2. Pixels are classified per class of MTMF classification.

N-D Class	Pixel per class	Element
1	603	Vegetation
2	637	Vegetation
3	1823	Biotite Granite
4	1803	Vegetation
5	1413	Fine Granite Lithium Mica Biotite and Tourmaline
6	293	Tourmaline Granite
7	269	Topaz Granite

4.5 SAM

In contrast to MTMF, the SAM algorithm did not classify the pixels uniformly. We can see from Figure 12, that the classification is not concentrated in specific points of the study area, but distributed over the entire area. The n-D class 3 (Biotite) presented classified pixels in dark red color that are mostly at the edge of the clusters. For minerals, this is the class that has the highest number of classified pixels (2832 pixels). Pixels in this class are most concentrated on the right side of the image (Biotite Granite) and center-left (mixed), and to a lesser extent in the center (Topaz Granite) and lower left (Tourmaline Granite). Class n-D 5 (various types of Granites) presents the highest amount of classified pixels (1530 pixels). This class is present throughout the study area, but to a lesser extent in the central region. The n-D class 6 (Tourmaline) is equally spread over the entire study area, but to a lesser extent than the previous two. It has the smallest amount of classified pixels and is more concentrated on the right side of the image, mainly in the Tourmaline Granite area. The n-D class 7 (Topaz) is also distributed throughout the study area, mainly in the lower left (Biotite Granite) but is isolated only in the central region (Topaz Granite). The number of unclassified pixels is high and exceeds all the other classes (36585 pixels). Among the unclassified elements are urban/artificial areas, exposed soil, water bodies, and roads. Table 3 shows the number of pixels classified in each class. Although the results are not as uniform as with the MTMF, the clusters formed by the SAM algorithm indicate the presence of minerals of interest and can be used in prospecting. Once a good analysis of mineral endmembers is collected, the presence of clusters formed by the respective minerals can be a good indication for prospecting.

Table 3. Pixels are classified per class of SAM classification.

N-D Class	Pixel per class	Element
0	36585	Unclassified
1	13991	Vegetation
2	1050	Vegetation
3	2832	Biotite Granite
4	5332	Vegetation
5	1530	Fine Granite, Lithium Mica, Biotite and Tourmaline
6	445	Tourmaline Granite
7	635	Topaz Granite

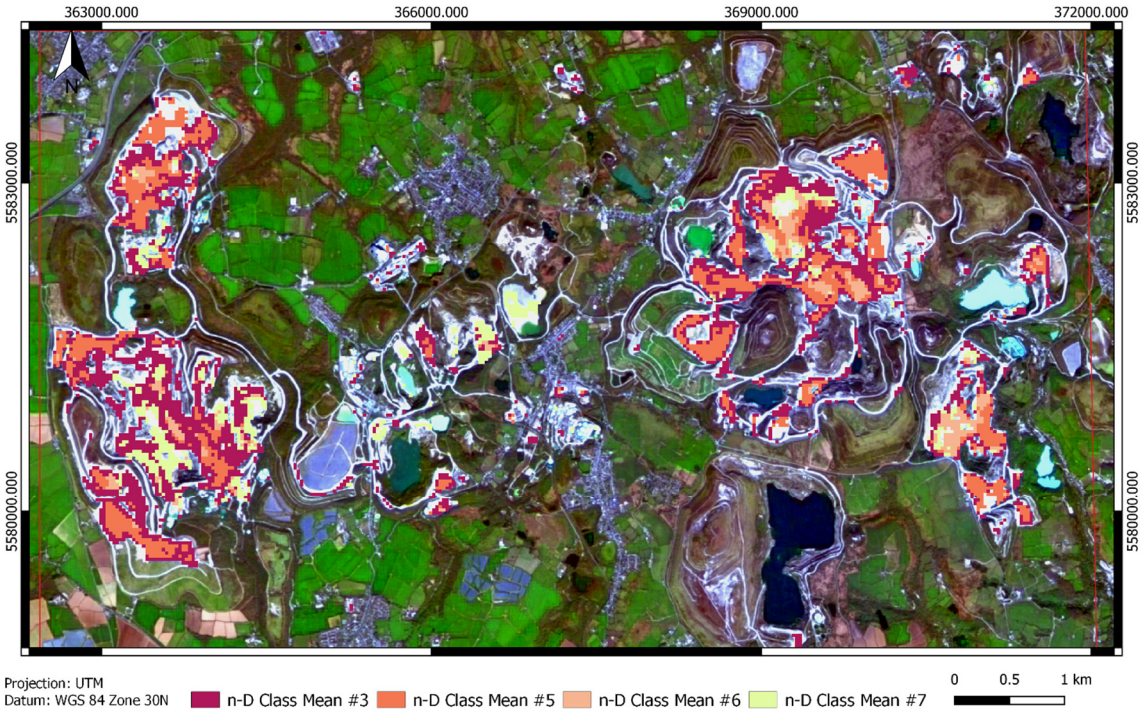

Figure 12. SAM classification results.

5. CONCLUSIONS

This research applied the SHW method on PRISMA hyperspectral images to verify its potential for the prospection of Li minerals. Clustering and selecting endmembers from the data cloud (n-D Visualiser) allowed to correctly select interest minerals. Despite the Spectral Analyst tool correctly identifying Kaolinite, this tool was unable to correctly identify other minerals. Because of this, a suplementary analysis was performed to compare the endmember and reference spectra in order to validate the results. This may be due to the low spectral variability of the pixels of the study area. The results indicate that Kaolinite is the predominant mineral in the study area. This makes sense, as it is the main mineral extracted in St. Austell China clay deposit. Despite this, the classification methods showed potential by forming clusters across the endmembers used as input to the classification process. Different clusters can be used as indirect indicators of the presence of Li minerals. In general, the MTMF classification result is superior to the SAM classification because it takes into account not only the spectral response, but also the spatial location of the selected endmembers. This suggests that it is the best option to measure the distribution and abundance of the interest minerals. In addition to being able to identify Kaolinite, the SHW method used proved capable of forming clusters that may indicate the presence of this mineral. This shows that PRISMA images have a great potential for prospecting research. In the future, this method can be applied to PRISMA hyperspectral images in an area with greater spectral variability to map the abundance of minerals of interest. This research makes an important contribution to the science of Li mineral prospecting, proving the potential of spectral unmixing-based methods applied to PRISMA images in identifying pathfinder minerals of interest for indirect prospecting. The results of this research are encouraging for the prospecting field, and the method applied proved to be efficient in mapping minerals. This method can be adapted to new study areas in the future.

ACKNOWLEDGMENTS

This study is funded by European Union's Horizon 2020 innovation program under grant agreement No 869274, project GREENPEG: New Exploration Tools for European Pegmatite Green-Tech Resources. The authors also acknowledge the financial support provided by Portuguese National Funds through the FCT – Fundação para a Ciência e a Tecnologia, I.P. (Portugal) projects UIDB/04683/2020 and UIDP/04683/2020 (Institute of Earth Sciences).

REFERENCES

[1] Vangi, E., D'amico, G., Francini, S., Giannetti, F., Lasserre, B., Marchetti, M. and Chirici, G., "The new hyperspectral satellite prisma: Imagery for forest types discrimination," Sensors (Switzerland) 21(4), 1–19 (2021).

[2] Stefano, P., Angelo, P., Simone, P., Filomena, R., Federico, S., Tiziana, S., Umberto, A., Vincenzo, C., Acito, N., Marco, D., Stefania, M., Giovanni, C., Raffaele, C., Roberto, D. B., Giovanni, L. and Cristina, A., "The PRISMA hyperspectral mission: Science activities and opportunities for agriculture and land monitoring," Present. IGARSS 2013 - 2013 IEEE Int. Geosci. Remote Sens. Symp., Institute of Electrical and Electronics Engineers (IEEE)., Melbourne, Australia (2013).

[3] Lazzeri, G., Frodella, W., Rossi, G. and Moretti, S., "Multitemporal Mapping of Post-Fire Land Cover Using Multiplatform PRISMA Hyperspectral and Sentinel-UAV Multispectral Data: Insights from Case Studies in Portugal and Italy," Sensors 21(12) (2021).

[4] Giardino, C., Bresciani, M., Braga, F., Fabbretto, A., Ghirardi, N., Pepe, M., Gianinetto, M., Colombo, R., Cogliati, S., Ghebrehiwot, S., Laanen, M. and Peters, S., "First Evaluation of PRISMA Level 1 Data for Water Applications," 20, 1–16 (2020).

[5] Cardoso-fernandes, J., Santos, D., Lima, A. and Teodoro, A. C., "ASSESSING THE PRISMA POTENTIAL FOR MINERAL EXPLORATION TO VECTOR LOW-GRADE LITHIUM DEPOSITS," Present. IGARSS 2022 - 2022 IEEE Int. Geosci. Remote Sens. Symp., Institute of Electrical and Electronics Engineers (IEEE), Kuala Lumpur, Malaysia (2022).

[6] Ellis, R. J. and Scott, P. W., "Evaluation of hyperspectral remote sensing as a means of environmental monitoring in the St. Austell China clay (kaolin) region, Cornwall, UK," Remote Sens. Environ. 93(1), 118–130 (2004).

[7] Mujabar, P. S. and Dajkumar, S., "Mapping of bauxite mineral deposits in the northern region of Saudi Arabia by using Advanced Spaceborne Thermal Emission and Reflection Radiometer satellite data," Geo-Spatial Inf. Sci. 22(1), 35–44 (2019).

[8] Manning, D. A. C., Hill, P. I. and Howe, J. H., "Primary lithological variation in the kaolinized St Austell Granite, Cornwall, England," J. Geol. Soc. London. 153(6), 827–838 (1996).

[9] Gabr, S., Ghulam, A. and Kusky, T., "Detecting areas of high-potential gold mineralization using ASTER data," Ore Geol. Rev. 38(1–2), 59–69 (2010).

[10] Psyrillos, A., Manning, D. A. C. and Burley, S. D., "GeocheMical constraints on kaolinization in the St Austell Granite, Cornwall, England," J. Geol. Soc. London. 155(5), 829–840 (1998).

[11] Guarini, R., Loizzo, R., Facchinetti, C., Longo, F., Ponticelli, B., Faraci, M., Dami, M., Cosi, M., Amoruso, L., Pasquale, V., Nicolo, T., Santoro, F., Colandrea, P., Miotti, E. and Di Nicolantonio, W., "Prisma Hyperspectral Mission Products," 2018, 179–182.

[12] Kokaly, R. F., Clark, R. N., Swayze, G. A., Livo, K. E., Hoefen, T. M., Pearson, N. C., Wise, R. A., Benzel, W. M., Lowers, H. A., Driscoll, R. L. and Klein, A. J., "USGS Spectral Library Version 7," Reston, VA (2017).

[13] L3Harris., "Spectral Hourglass Wizard," <https://www.l3harrisgeospatial.com/docs/spectralhourglasswizard.html> (7 October 2021).

[14] Odden, B., Itten, K. I. and Laboratories, R. S., "Implemented Comparison of a Hyperspectral Classification Method Imin Two Remote Sensing Software Packages," In: 6th Workshop on Imaging Spectroscopy, Tel Aviv, Israel (2009).

[15] Boardman, J. W., Kruse, F. a. and Green, R. O., "Mapping target signatures via partial unmixing of AVIRIS data," Summ. JPL Airborne Earth Sci. Work., 3–6 (1995).

[16] Wolfe, J. D. and Black, S. R., "Hyperspectral Analytics in ENVI - Target Detection and Spectral Mapping Methods" (2018).

[17] Rajendran, S. and Nasir, S., "Characterization of ASTER spectral bands for mapping of alteration zones of volcanogenic massive sulphide deposits," Ore Geol. Rev. 88, 317–335 (2017).

[18] Hu, B., Xu, Y., Wan, B., Wu, X. and Yi, G., "Hydrothermally altered mineral mapping using synthetic application of Sentinel-2A MSI, ASTER and Hyperion data in the Duolong area, Tibetan Plateau, China," Ore Geol. Rev. 101(July), 384–397 (2018).

[19] L3Harris., "The n-D Visualizer," <https://www.l3harrisgeospatial.com/docs/ndimensionalvisualizer.html> (11 November 2021).

[20] L3Harris., "Spectral Analyst," <https://www.l3harrisgeospatial.com/docs/spectralanalyst.html> (10 November 2021).

[21] L3Harris., "Mixture Tuned Matched Filtering," <https://www.l3harrisgeospatial.com/docs/mtmf.html> (2 November 2021).

[22] Kruse, F. A., Lefkoff, A. B., Boardman, J. W., Heidebrecht, K. B., Shapiro, A. T., Barloon, P. J. and Goetz, A. F. H., "The spectral image processing system (SIPS)—interactive visualization and analysis of imaging spectrometer data," Remote Sens. Environ. 44(2), 145–163 (1993).
[23] Panda, A. and Pradhan, D., "Hyperspectral image processing for target detection using Spectral Angle Mapping," 2015 Int. Conf. Ind. Instrum. Control. ICIC 2015(Icic), 1098–1103 (2015).
[24] HUETE, A. R., "11 - REMOTE SENSING FOR ENVIRONMENTAL MONITORING," [Environmental Monitoring and Characterization], J. F. Artiola, I. L. Pepper, and M. L. Brusseau, Eds., Academic Press, Burlington, 183–206 (2004).
[25] Cardoso-Fernandes, J., Silva, J., Dias, F., Lima, A., Teodoro, A. C., Barrès, O., Cauzid, J., Perrotta, M., Roda-Robles, E. and Ribeiro, M. A., "Tools for Remote Exploration: A Lithium (Li) Dedicated Spectral Library of the Fregeneda–Almendra Aplite–Pegmatite Field," Data 6(3) (2021).
[26] Cardoso-Fernandes, J., Silva, J., Lima, A., Teodoro, A. C., Perrotta, M., Cauzid, J. and Roda-Robles, E., "Characterization of Lithium (Li) minerals from the Fregeneda-Almendra region through laboratory spectral measurements: a comparative study," Earth Resour. Environ. Remote Sensing/GIS Appl. XI 11534, K. Schulz, Ed., 123–129, SPIE (2020).
[27] Cardoso-Fernandes, J., Silva, J., Lima, A., Teodoro, A. C., Perrotta, M., Cauzid, J., Roda-Robles, E. and Ribeiro, M. A., "Reflectance spectroscopy to validate remote sensing data/algorithms for satellite-based Lithium (Li) exploration (Central East Portugal)," Earth Resour. Environ. Remote Sensing/GIS Appl. XI 11534, K. Schulz, Ed., 115–122, SPIE (2020).
[28] Cardoso-Fernandes, J., Silva, J., Perrotta, M. M., Lima, A., Teodoro, A. C., Ribeiro, M. A., Dias, F., Barrès, O., Cauzid, J. and Roda-Robles, E., "Interpretation of the reflectance spectra of Lithium (Li) minerals and pegmatites: A case study for mineralogical and lithological identification in the fregeneda-almendra area," Remote Sens. 13(18) (2021).